

1 **Diurnal Cycle of IMERG V06 Precipitation**

2

3 **Jackson Tan^{1,2}, George J. Huffman², David T. Bolvin^{2,3}, and Eric J. Nelkin^{2,3}**

4 ¹Universities Space Research Association, Columbia, Maryland.

5 ²NASA Goddard Space Flight Center, Greenbelt, Maryland.

6 ³Science Systems and Applications, Inc., Lanham, Maryland.

7

8 Corresponding author: Jackson Tan (jackson.tan@nasa.gov)

9

10 **Key Points:**

- 11 • The maturity of the Integrated Multi-satellitE Retrievals for Global Precipitation
12 Measurement for diurnal cycle analysis is demonstrated
- 13 • Ground validation suggests that the diurnal cycle has a slight lag of generally no more
14 than an hour
- 15 • The high resolution, global coverage and long record allows an unprecedented view of
16 diurnal cycle around the world

17

18

19 **Abstract**

20 This study demonstrates the maturing ability of the half-hourly precipitation estimates from the
21 Integrated Multi-satellitE Retrievals for GPM (IMERG) for use in global analyses of the diurnal
22 cycle. The refined intercalibration and interpolation between the sensors in V06 leads to greater
23 consistency in the precipitation retrievals over different hours of the day. Evaluation against
24 ground measurements suggests a slight lag in the diurnal phase of only +0.59 h. We demonstrate
25 the diurnal cycle over different regions around the globe, including the Maritime Continent,
26 where accurate representation of precipitation variability in global models remains a challenge.
27 Using examples over Singapore, Bangladesh, and Lake Victoria, we reveal the intricate interplay
28 between diurnal and seasonal variability. This study demonstrates the unprecedented capability
29 of IMERG in capturing the diurnal cycle of precipitation globally, potentially advancing our
30 understanding in regions of sparse ground measurements and supporting improvements in its
31 representation in global models.

32 **Plain Language Summary**

33 Most people are familiar with afternoon thunderstorms in warm seasons or climates, which are a
34 common feature of the diurnal cycle of rainfall. Over the central US in summer, storms are more
35 likely in the middle of the night, while over ocean, rainfall tends to be highest in the early
36 morning. To study the diurnal cycle and the interplaying factors that drive them, many studies
37 have relied on satellite observations. Here, we demonstrate how refinements the latest NASA
38 GPM gridded precipitation product, IMERG V06, can lead to improved reliability for studying
39 diurnal cycles. With only a slight delay in time—an improvement over its predecessor—the
40 IMERG diurnal cycle reveals the time of day when rainfall is heaviest in the Maritime Continent,
41 a region in Southeast Asia where intricate coastlines and complex topography pose challenges to
42 global models. With a high resolution, long record, and global coverage, IMERG can quantify
43 the diurnal cycle of rainfall globally, from the small island of Singapore to the monsoon-
44 dominated Bangladesh to the sparsely measured Lake Victoria region in Africa. The maturing
45 ability of IMERG V06 in depicting the diurnal cycle of precipitation gives new confidence in
46 using these data for scientific studies.

47 **1 Introduction**

48 The diurnal cycle is one of the most prominent features of precipitation variability,
49 reflecting not just the local convective heating but also dynamical interactions between different
50 surface types and orography. Due to the challenges in representing such processes that span
51 across multiple spatiotemporal scales, global numerical models often struggle to represent the
52 diurnal cycle of precipitation accurately (e.g., Covey et al., 2016; Dai et al., 1999; Dai &
53 Trenberth, 2004), especially in regions such as the Maritime Continent where intricate coastlines
54 and topography accentuate the importance of local circulations between the land and the ocean
55 (Peatman et al., 2014; Qian, 2008; Worku et al., 2019). In many regions, sparse sub-daily ground
56 measurements limit our ability to characterize the local diurnal variability, especially over lakes
57 and oceans.

58 To overcome the limitation of sparse ground observations, some studies have used
59 satellite-based precipitation products to examine the diurnal variability (e.g., Dai et al., 2007;
60 Kikuchi & Wang, 2008; Watters & Battaglia, 2019; Worku et al., 2019). These products may be
61 based on active microwave retrievals (e.g., radar), which are generally more accurate but have

62 limited sampling, or merged passive microwave (PMW) and infrared (IR) retrievals, which have
63 wider coverage and higher time resolution but possess greater uncertainty, including possible
64 lags in diurnal phase. These studies generally find an afternoon peak over land and a morning
65 peak over ocean, a more pronounced cycle over land, and a greater reliability in the phase than
66 amplitude.

67 This study uses the IMERG V06 Final run product to examine the diurnal cycle of
68 precipitation, with the goal of demonstrating this dataset's maturing capability to advance our
69 understanding of diurnal variability globally and provide a basis for improving the representation
70 of the diurnal cycle in global models. Evaluation of earlier versions of IMERG suggested a lag in
71 phase but greater uncertainty in amplitude, with the precipitation amount better represented than
72 frequency and conditional precipitation rate (Li et al., 2018; Mayor et al., 2017; O & Kirstetter,
73 2018; Oliveira et al., 2016; Tang et al., 2016). Compared to previous V05, IMERG V06
74 possesses improved intercalibration and interpolation (Tan et al., 2019), leading to increased
75 confidence in its representation of the diurnal cycle. We will illustrate the improvement over
76 V05 and compare it with ground observations to quantify a residual lag in the diurnal cycle. We
77 will apply IMERG to several regions to reveal the intricate dependence of diurnal cycle on the
78 local conditions, possible even over small areas by virtue of the fine spatial resolution and robust
79 due to the long record.

80 **2 Data and Methods**

81 IMERG is the US merged satellite gridded precipitation product from the Global
82 Precipitation Measurement (GPM) mission that unifies observations from a network of partner
83 satellites in the GPM constellation (Huffman, Bolvin, Braithwaite, et al., 2019; Huffman, Bolvin,
84 Nelkin, et al., 2019; Precipitation Processing System, 2019a). Precipitation estimates are
85 provided at 0.1° grids every half-hour, between 60° latitudes for V05 and globally for V06. The
86 record for IMERG V05 begins in March 2014, while IMERG V06 extends this record back to
87 June 2000 (eventually to January 1998). IMERG has three runs—Early, Late, and Final—to
88 accommodate different user requirements for latency and accuracy. This study uses the gauge-
89 adjusted estimates from the Final runs of IMERG V05B and V06B, the latest versions of V05
90 and V06 respectively.

91 IMERG uses precipitation estimates derived from PMW sensors. The PMW precipitation
92 estimates are derived primarily from the Goddard Profiling algorithm (Kummerow et al., 2001,
93 2011, 2015; Precipitation Processing System, 2017), a fully-parametric retrieval algorithm that
94 estimates the surface precipitation rate from the PMW brightness temperature using a Bayesian
95 approach conditioned upon surface classes, surface temperature, and total precipitable water.
96 This retrieval algorithm is used for all PMW sensors except Sondeur Atmosphérique du Profil
97 d'Humidité Intertropicale par Radiométrie (SAPHIR), which uses the Precipitation Retrieval and
98 Profiling Scheme (Kidd, 2019; Precipitation Processing System, 2019b). The PMW estimates are
99 gridded to 0.1° every half-hour, and quasi-Lagrangian interpolation (known as “morphing”) is
100 applied to the gridded estimates to fill in gaps in the field using motion vectors computed from
101 total precipitable water vapor from numerical models in V06 and from geosynchronous IR
102 brightness temperatures in V05. The morphed precipitation is further supplemented, via a
103 Kalman filter approach following Joyce and Xie (2011), with microwave-calibrated IR
104 precipitation estimates using the Precipitation Estimation from Remotely-Sensed Information
105 from Artificial Neural Networks-Cloud Cluster System algorithm (Hong et al., 2004; Nguyen et

106 al., 2018). IMERG masks PMW and morphed estimates over frozen surfaces as depicted in the
107 NOAA AutoSnow product (Romanov et al., 2000), resulting in the use of IR precipitation within
108 60°N/S and missing values at high latitudes. The merged satellite estimates are then calibrated by
109 and merged with the Full and Monitoring surface gauge analyses from the Global Precipitation
110 Climatology Centre (Schneider et al., 2014, 2015) following the approach employed by Huffman
111 et al. (2007) for the Tropical Rainfall Measuring Mission (TRMM) Multisatellite Precipitation
112 Analysis (TMPA).

113 IMERG estimates are provided in UTC time. To obtain the mean precipitation rate as a
114 function of local solar time (LST), we first compute the mean precipitation rate at each half-hour
115 over a period sufficiently long to average out other modes of variability. We then convert the
116 UTC time to LST time based on its longitude (ranging from -180° to $+180^\circ$): LST hour = UTC
117 hour + longitude / 15, where the factor 15 represents the degree-longitude distance in an hour
118 and LST is rounded to the nearest half-hour.

119 To filter out noise and other possible modes of sub-daily variability in some of the
120 analyses, we utilize a low-pass filter on the mean precipitation rates as a function of LST. This is
121 especially useful if the precipitation rates are noisy, which is typical for fine-scale estimates.
122 Each use of the low-pass filter will be explicitly mentioned. The low-pass filter is achieved by
123 applying a fast Fourier transform, discarding components with frequencies above two cycles per
124 day, and inverting it back. This approach extracts the mean value, the diurnal cycle, and the
125 semidiurnal cycle, a process equivalent to a least square fit to the first and second harmonics
126 (Dai, 2001; O & Kirstetter, 2018).

127 **3 Improved Intersensor Calibration**

128 The PMW observations used in IMERG are provided by a host of different sensors on
129 board various satellite platforms. Due to vastly differing sensor properties, such as scan
130 strategies (conical versus cross-track), frequency channels, and footprint sizes, two sensors
131 viewing the same precipitation system may give different precipitation estimates even when the
132 same retrieval scheme is applied. While resolving instantaneous (i.e., random) differences
133 remains a major challenge, the intercalibration applied in IMERG is intended to remove the
134 mean (i.e., systematic) differences. This is especially pertinent in this study because most of
135 these satellite platforms fly in sun-synchronous orbits, so they observe precipitation at the same
136 two local times each day, although these times may change over the years due to satellite drift.
137 Therefore, when we analyze the diurnal cycle by averaging the precipitation rate at different
138 half-hours, any imperfections in the satellite intercalibrations will introduce artificial (i.e.,
139 instrument-induced) diurnal variability.

140 IMERG uses the Ku-band Combined Radar and Radiometer (CORRA) product as the
141 reference standard for calibration, with seasonal climatological adjustments to the Global
142 Precipitation Climatology Project V2.3 product (Adler et al., 2003, 2016) to control for known
143 deficiencies at certain latitudes. Ideally, all sensors would be directly calibrated to CORRA, but
144 coincident sampling is too sparse for partner sensors due to orbit characteristics and the narrow
145 swath of the CORRA estimates. Instead, the intercalibration is performed in two steps. First,
146 mean values of gridded partner sensors are adjusted to the GPM Microwave Imager (GMI) or
147 TRMM Microwave Imager (TMI) for the GPM and TRMM eras, respectively, using static
148 seasonal calibrations based on one year of coincident estimates. Second, GMI/TMI is calibrated
149 to CORRA using dynamic 45-day calibrations updated every 5 days, and this calibration is also

150 applied to the GMI/TMI-calibrated partner sensors. In V05, assumptions were made regarding
151 sensor characteristics, so only the Special Sensor Microwave Imager/Sounder sensors were
152 calibrated to GMI in the first step. For more details, see Huffman, Bolvin, Braithwaite, et al.
153 (2019).

154 To compare the magnitudes of artificial diurnal variability, we show the mean
155 precipitation rate from IMERG V05B and V06B as a function of LST over the Southern Ocean
156 latitudes (40–60°S) in Figure 1, limited to the period between December 2014 and February
157 2015 to minimize effects of satellite drift. Absent station-keeping, the satellite would drift,
158 gradually changing the LST hour of a sun-synchronous sensor overpass, which—while desirable
159 for analysis of the diurnal cycle—would limit our ability to isolate the effects of intersensor
160 differences and interpolation. In this region, actual diurnal variability is relatively muted, so any
161 high frequency variation across the LST is likely attributable to deficiencies in intercalibration.
162 Indeed, V05B and V06B display variations across the LST, but this variability is reduced in
163 V06B. In particular, the spikes in the mean precipitation rate associated with the MHS, which
164 may be misinterpreted as semidiurnal signals, are reduced considerably. This improved
165 instrumental consistency is also evident in other regions (Figure S1). Therefore, the improved
166 intercalibration in V06B allows for a more consistent precipitation retrieval over different times
167 of the day for diurnal cycle analysis.

168 In addition, IMERG V06 introduced a morphing scheme based on total precipitable water
169 vapor from numerical models, which tests show to be an improvement over the previous IR-
170 based scheme, especially in these Southern Ocean latitudes (Tan et al., 2019). In terms of its
171 impact on diurnal cycle, this will lead to less artificial variability during times that are only
172 occasionally sampled by non-sun-synchronous PMW satellites such as GMI. Indeed, from LST
173 hour 10 to 13 when there is a long gap between successive sun-synchronous PMW overpasses,
174 the mean precipitation rate in V06B is constant (Figure 1). In contrast, the mean precipitation
175 rate in V05B has considerable variability, including a minimum at hour 12. Hence, the new
176 morphing scheme creates a more consistent precipitation rate between PMW observations
177 through a smoother interpolation.

178 **4 Evaluation of the IMERG V06 Diurnal Cycle**

179 Ground validation of diurnal variability for satellite-based precipitation products often
180 identifies a lag in phase. Here, we use a version of the Multi-Radar Multi-Sensor (MRMS)—a
181 US radar- and gauge-based product—processed for GPM ground validation (Kirstetter et al.,
182 2012, 2014, 2015) to evaluate the diurnal cycle in IMERG. Figure 2a and b examines the diurnal
183 phase by showing the LST time of the peak in the low-pass filtered mean precipitation rate
184 between IMERG and MRMS, respectively, for June-July-August from 2014 to 2018. Broadly
185 speaking, the times of the diurnal peak in precipitation are comparable. In particular, the
186 eastward propagation of nocturnal mesoscale convective systems in the central US—a distinctive
187 feature of summertime precipitation in this region (e.g., Carbone & Tuttle, 2008)—is well
188 captured by IMERG. Likewise, IMERG identifies the conspicuous afternoon peak in
189 precipitation in the southeastern US, a region with a prominent diurnal cycle of convection
190 amidst a general absence of strong orography. In the Gulf of Mexico near the coast, IMERG is
191 able to discern the late morning peak in precipitation due to near-surface wind convergence
192 (Virts et al., 2015). In the southwestern US, there is a distinct lag in the peak time of IMERG,

193 though the aridity of this region may limit the robustness of this result due to weaker diurnal
194 variability.

195 Focusing on the southeast US due to its strong diurnal cycle and reliable radar coverage,
196 Figure 2c shows the histogram of the difference in peak times between IMERG and MRMS of
197 the grid boxes in the region outlined in Figure 2a and b. The majority of the pixels are distributed
198 near zero with a small offset towards the positive. The mean difference in peak time between
199 IMERG and MRMS is +0.59 h, with a median of +0.5 h and an interquartile range of 0 h to +1.0
200 h. This indicates that IMERG peaks at a time close to MRMS but with a slight lag, though no
201 more than an hour for at least half the points. A similar analysis for the central US nocturnal
202 convection showed a comparable lag (Figure S2). Such a lag can be attributed to the delay in the
203 falling hydrometeors at the level of the ice-scattering signal aloft as observed by the PMW
204 sensors to the surface (e.g., Tan et al., 2018; You et al., 2019). This result contrasts with IR-
205 based precipitation, which has a higher mean lag of +1.48 h (Figure S3), likely because IR
206 observes the cloud tops that are at a higher altitude. In fact, the legacy TRMM multi-satellite
207 precipitation product, TMPA, typically possesses a larger diurnal lag (e.g., Kikuchi & Wang,
208 2008), which is partly due to its greater IR contribution and exacerbated by its coarser time
209 resolution of 3 h. While IMERG uses IR precipitation, the contribution is much lower than in
210 TMPA due to the use of morphing for interpolating between PMW observations, so the lag
211 largely reflects the lag of PMW retrievals.

212 The discussion in this section thus far focused on diurnal phase; Figure 2d includes an
213 assessment of the diurnal amplitude by showing the mean precipitation rate of the same
214 southeastern states as Figure 2c. Apart from the slight lag, IMERG also underestimates the
215 amplitude of the mean precipitation rate in this region compared to MRMS, consistent with the
216 results of O and Kirstetter (2018) and Figure S4, both of which conversely also observed
217 overestimation in other regions. Given that the mean precipitation rate is lower in IMERG than
218 in MRMS at most times of the day in Figure 2d, this suggests that the gauges used in the IMERG
219 bias adjustment may be underestimating the amount of precipitation. Since the gauge adjustment
220 technique is identical between V06B and previous versions, we refer readers to O and Kirstetter
221 (2018) for a more comprehensive evaluation of diurnal amplitude. Figure 2d also includes both
222 the unfiltered and low-pass filtered precipitation rates, which indicate that the low-pass filter may
223 modify the diurnal amplitude but not the phase (Watters & Battaglia, 2019). The mean IMERG
224 precipitation rates over different years vary in diurnal amplitude to some degree, but the diurnal
225 phase is generally consistent (Figure S5).

226 **5 Global Diurnal Cycle**

227 The general consistency of the IMERG diurnal phase against ground observations, with a
228 slight lag of generally no more than one hour, encourages us to examine IMERG in other regions
229 of the world with strong diurnal cycles. One such region is the Maritime Continent, where the
230 intense tropical heating and complex coastlines result in an intricate diurnal pattern that is often
231 challenging for global weather and climate models to represent accurately (e.g., Gianotti et al.,
232 2012; Neale & Slingo, 2003; Qian, 2008).

233 Figure 3 shows the time of the peak in the low-pass filtered mean IMERG precipitation
234 rate over the Maritime Continent for March-April-May (MAM) of 2001–2018, a season selected
235 for the lack of monsoon precipitation that would otherwise reduce the prominence of the diurnal
236 variability. The diurnal cycle is distinct over land but noisier over oceanic areas far from land, a

237 reflection of the weaker influence of convection over ocean compared to other factors, including
238 artificial diurnal variability (Figure 1). Precipitation reaches a peak in the afternoon over land
239 near the coast, and in the late afternoon or evening further inland. Over ocean, maximum
240 precipitation occurs around midnight close to the shore, and in the morning further offshore. This
241 is consistent with other studies using active retrievals and ground observations (e.g., Mori et al.,
242 2004). The time of peak precipitation over different surface type varies as a function of the
243 distance from the coast, indicating the importance of land-sea breezes and gravity waves in
244 modulating precipitation in this region (e.g., Birch et al., 2016; Hassim et al., 2016; Sato et al.,
245 2009; Yokoi et al., 2017). While previous studies have used products such as TMPA to probe the
246 diurnal cycle in the Maritime Continent (e.g., Kikuchi & Wang, 2008; Rauniyar et al., 2017;
247 Worku et al., 2019), the lower lag and higher time resolution of IMERG reveals a more intricate
248 and refined picture of diurnal phase.

249 The high spatial resolution of IMERG allows us to study regions of limited area, and its
250 long record enables us to construct a robust diurnal profile by increasing the number of
251 observations. To illustrate this capability, we plot the mean precipitation rate over Singapore
252 (Figure 4a), where only the centers of three grid boxes fall within its boundary (see Text S1 on
253 method and Figure S6 on boundary). While there is still some noise in the mean precipitation
254 rate, the diurnal variability is clear. The afternoon peak in convection is evident across all four
255 seasons. Furthermore, for September-October-November (SON), there is a secondary peak in the
256 morning, which is likely caused by the eastward propagating Sumatra Squalls (Lo & Orton,
257 2016). Seasonal variability over Singapore is weak, with only the precipitation rates of June-
258 July-August (JJA) being appreciably lower due to the dry southwesterly monsoon.

259 As a contrast to this strong diurnal variability, Figure 4b shows the mean precipitation
260 rate over Bangladesh (Figure S7), a subtropical Asian country but with a markedly different
261 climatology. Here, diurnal variability is more subdued; instead, there is a very strong seasonal
262 cycle associated with the monsoon. Unlike the southwesterly monsoon in Singapore, which is
263 dry due to the mountains in Sumatra, the southwesterly monsoon arrives in Bangladesh
264 unimpeded from the Indian Ocean in JJA, producing copious rainfall throughout all times of the
265 day with two distinct peaks (Islam & Uyeda, 2006). In contrast, the northeasterly monsoon
266 originating from the Asian continent is dry and suppresses precipitation in December-January-
267 February (DJF).

268 One key advantage of satellite-based precipitation products such as IMERG is their
269 ability to provide estimates over water, where surface observations are sparse and infrequent.
270 Figure 4c shows the mean precipitation rate over Lake Victoria (Figure S8), the largest of the
271 African Great Lakes, where there is both diurnal variability and seasonal variability. In JJA, the
272 Intertropical Convergence Zone migrates northwards away from the region, leading to less
273 precipitation over the lake. Precipitation is greater in other seasons, with the heaviest rainfall
274 occurring in MAM. In terms of diurnal variability, precipitation is greatest in the morning driven
275 by land-lake breeze, evaporation, and katabatic winds originating from surrounding topography
276 (Anyah et al., 2006; Thiery et al., 2015). However, in MAM, the timing of peak precipitation
277 shifts several hours earlier in the morning, with substantial precipitation falling in the hours
278 before midnight.

279 **6 Conclusions**

280 This study demonstrated the maturing ability of the improved IMERG in depicting the
281 diurnal cycle of precipitation around the world. An analysis over the Southern Ocean showed
282 that the improved intercalibration and interpolation in V06 reduced artificial diurnal variability
283 compared to V05. Evaluation against US ground observations shows broad agreements and
284 suggests a slight lag in the diurnal phase—but generally no more than an hour—and regional
285 differences in the diurnal amplitude. Applying IMERG to the Maritime Continent revealed an
286 intricate pattern in the time of the day that the precipitation peaks and thus the importance of
287 land-sea breezes in modulating diurnal variability. Analyses leveraging the fine resolution and
288 long record of IMERG over Singapore, Bangladesh, and Lake Victoria illustrated the interplay
289 between diurnal and seasonal cycles, exemplifying the unprecedented ability of IMERG in
290 capturing the diurnal variability of precipitation globally.

291 In the comparison against ground observations, the 0 to +1 h lag in diurnal phase of
292 IMERG over land is an improvement over the longer lag in TMPA, primarily due to the
293 increased contribution from PMW and use of morphing, though the former advantage diminishes
294 in the earlier IMERG record. This improvement in lag is consistent with other studies (e.g.,
295 Dezfuli et al., 2017; O & Kirstetter, 2018) and its magnitude is similar to the +40 min offset in O
296 et al. (2017) and the +30 min lag in You et al. (2019). On the other hand, over ocean, PMW
297 retrievals rely on the emission signal of both the solid and liquid hydrometeors, with the latter
298 being closer to the surface. Therefore, we expect any lag due to fall delay in the diurnal phase of
299 IMERG over the ocean to be even lower than the average of +0.59 h over southeastern US.

300 Accurate representations of diurnal cycles of precipitation by global weather and climate
301 models generally remain an ongoing goal. At the same time, sparse sub-daily ground
302 observations limit our ability to understand the diurnal cycles in many regions around the world.
303 The results in this study suggest that IMERG has the potential to advance our understanding in
304 regions of sparse ground measurements and complement ongoing efforts to improve its
305 representation in global models (Covey et al., 2016; Tapiador et al., 2017, 2019; Xie et al.,
306 2018).

307 **Acknowledgments, Samples, and Data**

308 The authors thank two anonymous reviewers and the editor Kaicun Wang for their detailed
309 comments that improved this study. The authors also benefited from discussions with Wim
310 Theyry and Elise Monsieurs. IMERG was provided by the NASA Goddard Space Flight Center's
311 IMERG and PPS teams, which develop and compute IMERG as a contribution to the GPM
312 mission, and archived at the NASA GES DISC
313 (https://disc.gsfc.nasa.gov/datasets/GPM_3IMERGHH_V06/summary) and at
314 <https://pmm.nasa.gov/data-access/download/gpm>. All authors are supported by the NASA
315 Precipitation Measurement Missions funding (NNH18ZDA001N-PMMST). Codes used to
316 perform the analysis in this study can be obtained online at
317 https://github.com/JacksonTanBS/2019_GRL_IMERGdiurnal.

318 **References**

319 Adler, R. F., Huffman, G. J., Chang, A., Ferraro, R., Xie, P.-P., Janowiak, J., et al. (2003). The
320 version-2 global precipitation climatology project (GPCP) monthly precipitation analysis

321 (1979-present). *Journal of Hydrometeorology*, 4(6), 1147–1167.
322 [https://doi.org/10.1175/1525-7541\(2003\)004<1147:TVGPCP>2.0.CO;2](https://doi.org/10.1175/1525-7541(2003)004<1147:TVGPCP>2.0.CO;2)

323 Adler, R. F., Wang, J.-J., Sapiano, M., Huffman, G., Chiu, L., Xie, P. P., et al. (2016). Global
324 Precipitation Climatology Project (GPCP) Climate Data Record (CDR), Version 2.3
325 (Monthly) [Data set]. NOAA National Centers for Environmental Information.
326 <https://doi.org/10.7289/v56971m6>

327 Anyah, R. O., Semazzi, F. H. M., & Xie, L. (2006). Simulated Physical Mechanisms Associated
328 with Climate Variability over Lake Victoria Basin in East Africa. *Monthly Weather*
329 *Review*, 134(12), 3588–3609. <https://doi.org/10.1175/MWR3266.1>

330 Birch, C. E., Webster, S., Peatman, S. C., Parker, D. J., Matthews, A. J., Li, Y., & Hassim, M. E.
331 E. (2016). Scale Interactions between the MJO and the Western Maritime Continent.
332 *Journal of Climate*, 29(7), 2471–2492. <https://doi.org/10.1175/JCLI-D-15-0557.1>

333 Carbone, R. E., & Tuttle, J. D. (2008). Rainfall Occurrence in the U.S. Warm Season: The
334 Diurnal Cycle. *Journal of Climate*, 21(16), 4132–4146.
335 <https://doi.org/10.1175/2008JCLI2275.1>

336 Covey, C., Gleckler, P. J., Doutriaux, C., Williams, D. N., Dai, A., Fasullo, J., et al. (2016).
337 Metrics for the Diurnal Cycle of Precipitation: Toward Routine Benchmarks for Climate
338 Models. *Journal of Climate*, 29(12), 4461–4471. <https://doi.org/10.1175/JCLI-D-15-0664.1>

340 Dai, A. (2001). Global Precipitation and Thunderstorm Frequencies. Part II: Diurnal Variations.
341 *Journal of Climate*, 14(6), 1112–1128. [https://doi.org/10.1175/1520-0442\(2001\)014<1112:GPATFP>2.0.CO;2](https://doi.org/10.1175/1520-0442(2001)014<1112:GPATFP>2.0.CO;2)

343 Dai, A., & Trenberth, K. E. (2004). The Diurnal Cycle and Its Depiction in the Community
344 Climate System Model. *Journal of Climate*, 17(5), 930–951.
345 [https://doi.org/10.1175/1520-0442\(2004\)017<0930:TDCALD>2.0.CO;2](https://doi.org/10.1175/1520-0442(2004)017<0930:TDCALD>2.0.CO;2)

346 Dai, A., Giorgi, F., & Trenberth, K. E. (1999). Observed and model-simulated diurnal cycles of
347 precipitation over the contiguous United States. *Journal of Geophysical Research:*
348 *Atmospheres*, 104(D6), 6377–6402. <https://doi.org/10.1029/98JD02720>

349 Dai, A., Lin, X., & Hsu, K.-L. (2007). The frequency, intensity, and diurnal cycle of
350 precipitation in surface and satellite observations over low- and mid-latitudes. *Climate*
351 *Dynamics*, 29(7–8), 727–744. <https://doi.org/10.1007/s00382-007-0260-y>

352 Dezfuli, A. K., Ichoku, C. M., Huffman, G. J., Mohr, K. I., Selker, J. S., van de Giesen, N., et al.
353 (2017). Validation of IMERG Precipitation in Africa. *Journal of Hydrometeorology*,
354 18(10), 2817–2825. <https://doi.org/10.1175/JHM-D-17-0139.1>

355 Gianotti, R. L., Zhang, D., & Eltahir, E. A. B. (2012). Assessment of the Regional Climate
356 Model Version 3 over the Maritime Continent Using Different Cumulus Parameterization
357 and Land Surface Schemes. *Journal of Climate*, 25(2), 638–656.
358 <https://doi.org/10.1175/JCLI-D-11-00025.1>

359 Hassim, M. E. E., Lane, T. P., & Grabowski, W. W. (2016). The diurnal cycle of rainfall over
360 New Guinea in convection-permitting WRF simulations. *Atmospheric Chemistry and*
361 *Physics*, 16(1), 161–175. <https://doi.org/10.5194/acp-16-161-2016>

- 362 Hong, Y., Hsu, K.-L., Sorooshian, S., & Gao, X. (2004). Precipitation Estimation from Remotely
363 Sensed Imagery Using an Artificial Neural Network Cloud Classification System.
364 *Journal of Applied Meteorology*, 43(12), 1834–1853. <https://doi.org/10.1175/JAM2173.1>
- 365 Huffman, G. J., Bolvin, D. T., Nelkin, E. J., Wolff, D. B., Adler, R. F., Gu, G., et al. (2007). The
366 TRMM Multisatellite Precipitation Analysis (TMPA): Quasi-Global, Multiyear,
367 Combined-Sensor Precipitation Estimates at Fine Scales. *Journal of Hydrometeorology*,
368 8(1), 38–55. <https://doi.org/10.1175/JHM560.1>
- 369 Huffman, G. J., Bolvin, D. T., Braithwaite, D., Hsu, K., Joyce, R., Kidd, C., et al. (2019).
370 *Algorithm Theoretical Basis Document (ATBD) Version 06. NASA Global Precipitation*
371 *Measurement (GPM) Integrated Multi-satellitE Retrievals for GPM (IMERG) (Algorithm*
372 *Theoretical Basis Document)* (p. 38). NASA. Retrieved from [https://pmm.nasa.gov/data-](https://pmm.nasa.gov/data-access/downloads/gpm)
373 [access/downloads/gpm](https://pmm.nasa.gov/data-access/downloads/gpm)
- 374 Huffman, G. J., Bolvin, D. T., Nelkin, E. J., & Tan, J. (2019). *Integrated Multi-satellitE*
375 *Retrievals for GPM (IMERG) Technical Documentation* (Technical Documentation) (p.
376 71). NASA. Retrieved from <https://pmm.nasa.gov/data-access/downloads/gpm>
- 377 Islam, M., & Uyeda, H. (2006). TRMM Observed Vertical Structure and Diurnal Variation of
378 Precipitation in South Asia. In *2006 IEEE International Symposium on Geoscience and*
379 *Remote Sensing* (pp. 1292–1295). Denver, CO, USA: IEEE.
380 <https://doi.org/10.1109/IGARSS.2006.334>
- 381 Joyce, R. J., & Xie, P. (2011). Kalman Filter–Based CMORPH. *Journal of Hydrometeorology*,
382 12(6), 1547–1563. <https://doi.org/10.1175/JHM-D-11-022.1>
- 383 Kidd, C. (2019). *Algorithm Theoretical Basis Document (ATBD) Version 01-02. NASA Global*
384 *Precipitation Measurement (GPM) Precipitation Retrieval and Profiling Scheme (PRPS)*
385 (Algorithm Theoretical Basis Document). NASA. Retrieved from
386 <https://pmm.nasa.gov/data-access/downloads/gpm>
- 387 Kikuchi, K., & Wang, B. (2008). Diurnal Precipitation Regimes in the Global Tropics. *Journal*
388 *of Climate*, 21(11), 2680–2696. <https://doi.org/10.1175/2007JCLI2051.1>
- 389 Kirstetter, P.-E., Hong, Y., Gourley, J. J., Chen, S., Flamig, Z., Zhang, J., et al. (2012). Toward a
390 Framework for Systematic Error Modeling of Spaceborne Precipitation Radar with
391 NOAA/NSSL Ground Radar–Based National Mosaic QPE. *Journal of*
392 *Hydrometeorology*, 13(4), 1285–1300. <https://doi.org/10.1175/JHM-D-11-0139.1>
- 393 Kirstetter, P.-E., Hong, Y., Gourley, J. J., Cao, Q., Schwaller, M., & Petersen, W. (2014).
394 Research Framework to Bridge from the Global Precipitation Measurement Mission Core
395 Satellite to the Constellation Sensors Using Ground-Radar-Based National Mosaic QPE.
396 In V. Lakshmi, D. Alsdorf, M. Anderson, S. Biancamaria, M. Cosh, J. Entin, et al. (Eds.),
397 *Remote Sensing of the Terrestrial Water Cycle, Geophysical Monograph 206* (pp. 61–
398 79). Hoboken, NJ: John Wiley & Sons, Inc.
- 399 Kirstetter, P.-E., Gourley, J. J., Hong, Y., Zhang, J., Moazamigoodarzi, S., Langston, C., &
400 Arthur, A. (2015). Probabilistic precipitation rate estimates with ground-based radar
401 networks. *Water Resources Research*, 51, 1422–1442.
402 <https://doi.org/10.1002/2014WR015672>

- 403 Kummerow, C. D., Hong, Y., Olson, W. S., Yang, S., Adler, R. F., McCollum, J., et al. (2001).
404 The Evolution of the Goddard Profiling Algorithm (GPROF) for Rainfall Estimation
405 from Passive Microwave Sensors. *Journal of Applied Meteorology*, 40(11), 1801–1820.
406 [https://doi.org/10.1175/1520-0450\(2001\)040<1801:TEOTGP>2.0.CO;2](https://doi.org/10.1175/1520-0450(2001)040<1801:TEOTGP>2.0.CO;2)
- 407 Kummerow, C. D., Ringerud, S., Crook, J., Randel, D., & Berg, W. (2011). An Observationally
408 Generated A Priori Database for Microwave Rainfall Retrievals. *Journal of Atmospheric
409 and Oceanic Technology*, 28(2), 113–130. <https://doi.org/10.1175/2010JTECHA1468.1>
- 410 Kummerow, C. D., Randel, D. L., Kulie, M., Wang, N.-Y., Ferraro, R., Joseph Munchak, S., &
411 Petkovic, V. (2015). The Evolution of the Goddard Profiling Algorithm to a Fully
412 Parametric Scheme. *Journal of Atmospheric and Oceanic Technology*, 32(12), 2265–
413 2280. <https://doi.org/10.1175/JTECH-D-15-0039.1>
- 414 Li, R., Wang, K., & Qi, D. (2018). Validating the Integrated Multisatellite Retrievals for Global
415 Precipitation Measurement in Terms of Diurnal Variability With Hourly Gauge
416 Observations Collected at 50,000 Stations in China. *Journal of Geophysical Research:
417 Atmospheres*, 123(18), 10,423–10,442. <https://doi.org/10.1029/2018JD028991>
- 418 Lo, J. C.-F., & Orton, T. (2016). The general features of tropical Sumatra Squalls. *Weather*,
419 71(7), 175–178. <https://doi.org/10.1002/wea.2748>
- 420 Mayor, Y., Tereshchenko, I., Fonseca-Hernández, M., Pantoja, D., & Montes, J. (2017).
421 Evaluation of Error in IMERG Precipitation Estimates under Different Topographic
422 Conditions and Temporal Scales over Mexico. *Remote Sensing*, 9(6), 503.
423 <https://doi.org/10.3390/rs9050503>
- 424 Mori, S., Jun-Ichi, H., Tauhid, Y. I., Yamanaka, M. D., Okamoto, N., Murata, F., et al. (2004).
425 Diurnal Land–Sea Rainfall Peak Migration over Sumatera Island, Indonesian Maritime
426 Continent, Observed by TRMM Satellite and Intensive Rawinsonde Soundings. *Monthly
427 Weather Review*, 132(8), 2021–2039. [https://doi.org/10.1175/1520-
428 0493\(2004\)132<2021:DLRPMO>2.0.CO;2](https://doi.org/10.1175/1520-0493(2004)132<2021:DLRPMO>2.0.CO;2)
- 429 Neale, R., & Slingo, J. (2003). The maritime continent and its role in the global climate: A GCM
430 study. *Journal of Climate*, 16(5), 834–848. [https://doi.org/10.1175/1520-
431 0442\(2003\)016<0834:TMCAIR>2.0.CO;2](https://doi.org/10.1175/1520-0442(2003)016<0834:TMCAIR>2.0.CO;2)
- 432 Nguyen, P., Ombadi, M., Sorooshian, S., Hsu, K., AghaKouchak, A., Braithwaite, D., et al.
433 (2018). The PERSIANN family of global satellite precipitation data: a review and
434 evaluation of products. *Hydrology and Earth System Sciences*, 22(11), 5801–5816.
435 <https://doi.org/10.5194/hess-22-5801-2018>
- 436 O, S., & Kirstetter, P. (2018). Evaluation of diurnal variation of GPM IMERG-derived summer
437 precipitation over the contiguous US using MRMS data. *Quarterly Journal of the Royal
438 Meteorological Society*, 144(S1), 270–281. <https://doi.org/10.1002/qj.3218>
- 439 O, S., Foelsche, U., Kirchengast, G., Fuchsberger, J., Tan, J., & Petersen, W. A. (2017).
440 Evaluation of GPM IMERG Early, Late, and Final rainfall estimates using WegenerNet
441 gauge data in southeastern Austria. *Hydrology and Earth System Sciences*, 21(12), 6559–
442 6572. <https://doi.org/10.5194/hess-21-6559-2017>

- 443 Oliveira, R., Maggioni, V., Vila, D., & Morales, C. (2016). Characteristics and Diurnal Cycle of
444 GPM Rainfall Estimates over the Central Amazon Region. *Remote Sensing*, 8(7), 544.
445 <https://doi.org/10.3390/rs8070544>
- 446 Peatman, S. C., Matthews, A. J., & Stevens, D. P. (2014). Propagation of the Madden-Julian
447 Oscillation through the Maritime Continent and scale interaction with the diurnal cycle of
448 precipitation: MJO Propagation and Scale Interaction with the Diurnal Cycle. *Quarterly*
449 *Journal of the Royal Meteorological Society*, 140(680), 814–825.
450 <https://doi.org/10.1002/qj.2161>
- 451 Precipitation Processing System. (2017). GPM GMI (GPROF) Radiometer Precipitation
452 Profiling L2A 1.5 hours 13 km V05 [Data set]. NASA Goddard Earth Sciences Data and
453 Information Services Center. <https://doi.org/10.5067/gpm/gmi/gpm/gprof/2a/05>
- 454 Precipitation Processing System. (2019a). GPM IMERG Final Precipitation L3 Half Hourly 0.1
455 degree x 0.1 degree V06 [Data set]. NASA Goddard Earth Sciences Data and Information
456 Services Center. <https://doi.org/10.5067/gpm/imerg/3b-hh/06>
- 457 Precipitation Processing System. (2019b). GPM SAPHIR on MT1 (PRPS) Radiometer
458 Precipitation Profiling L2 1.5 hours 10 km V06 [Data set]. NASA Goddard Earth
459 Sciences Data and Information Services Center.
460 <https://doi.org/10.5067/gpm/saphir/mt1/prps/2a/06>
- 461 Qian, J.-H. (2008). Why Precipitation Is Mostly Concentrated over Islands in the Maritime
462 Continent. *Journal of the Atmospheric Sciences*, 65(4), 1428–1441.
463 <https://doi.org/10.1175/2007JAS2422.1>
- 464 Rauniyar, S. P., Protat, A., & Kanamori, H. (2017). Uncertainties in TRMM-Era multisatellite-
465 based tropical rainfall estimates over the Maritime Continent: Uncertainties in SBR
466 Rainfall Estimates. *Earth and Space Science*, 4(5), 275–302.
467 <https://doi.org/10.1002/2017EA000279>
- 468 Romanov, P., Gutman, G., & Csiszar, I. (2000). Automated Monitoring of Snow Cover over
469 North America with Multispectral Satellite Data. *Journal of Applied Meteorology*,
470 39(11), 1866–1880. [https://doi.org/10.1175/1520-
471 0450\(2000\)039<1866:AMOSCO>2.0.CO;2](https://doi.org/10.1175/1520-0450(2000)039<1866:AMOSCO>2.0.CO;2)
- 472 Sato, T., Miura, H., Satoh, M., Takayabu, Y. N., & Wang, Y. (2009). Diurnal Cycle of
473 Precipitation in the Tropics Simulated in a Global Cloud-Resolving Model. *Journal of*
474 *Climate*, 22(18), 4809–4826. <https://doi.org/10.1175/2009JCLI2890.1>
- 475 Schneider, U., Becker, A., Finger, P., Meyer-Christoffer, A., Ziese, M., & Rudolf, B. (2014).
476 GPCP's new land surface precipitation climatology based on quality-controlled in situ
477 data and its role in quantifying the global water cycle. *Theoretical and Applied*
478 *Climatology*, 115(1–2), 15–40. <https://doi.org/10.1007/s00704-013-0860-x>
- 479 Schneider, U., Becker, A., Finger, P., Meyer-Christoffer, A., Rudolf, B., & Ziese, M. (2015).
480 GPCP Full Data Reanalysis Version 7.0 at 1.0°: Monthly Land-Surface Precipitation
481 from Rain-Gauges built on GTS-based and Historic Data: Gridded Monthly Totals [Data
482 set]. Global Precipitation Climatology Centre (GPCC) at Deutscher Wetterdienst.
483 https://doi.org/10.5676/dwd_gpcc/fd_m_v7_100

- 484 Tan, J., Petersen, W. A., Kirchengast, G., Goodrich, D. C., & Wolff, D. B. (2018). Evaluation of
485 Global Precipitation Measurement Rainfall Estimates against Three Dense Gauge
486 Networks. *Journal of Hydrometeorology*, *19*(3), 517–532. [https://doi.org/10.1175/JHM-](https://doi.org/10.1175/JHM-D-17-0174.1)
487 [D-17-0174.1](https://doi.org/10.1175/JHM-D-17-0174.1)
- 488 Tan, J., Huffman, G. J., Bolvin, D. T., & Nelkin, E. J. (2019). IMERG V06: Changes to the
489 Morphing Algorithm. *Journal of Atmospheric and Oceanic Technology*, *in press*.
490 <https://doi.org/10.1175/JTECH-D-19-0114.1>
- 491 Tang, G., Ma, Y., Long, D., Zhong, L., & Hong, Y. (2016). Evaluation of GPM Day-1 IMERG
492 and TMPA Version-7 legacy products over Mainland China at multiple spatiotemporal
493 scales. *Journal of Hydrology*, *533*, 152–167.
494 <https://doi.org/10.1016/j.jhydrol.2015.12.008>
- 495 Tapiador, F. J., Navarro, A., Levizzani, V., García-Ortega, E., Huffman, G. J., Kidd, C., et al.
496 (2017). Global precipitation measurements for validating climate models. *Atmospheric*
497 *Research*, *197*, 1–20. <https://doi.org/10.1016/j.atmosres.2017.06.021>
- 498 Tapiador, F. J., Roca, R., Del Genio, A., Dewitte, B., Petersen, W., & Zhang, F. (2019). Is
499 Precipitation a Good Metric for Model Performance? *Bulletin of the American*
500 *Meteorological Society*, *100*(2), 223–233. <https://doi.org/10.1175/BAMS-D-17-0218.1>
- 501 Thiery, W., Davin, E. L., Panitz, H.-J., Demuzere, M., Lhermitte, S., & van Lipzig, N. (2015).
502 The Impact of the African Great Lakes on the Regional Climate. *Journal of Climate*,
503 *28*(10), 4061–4085. <https://doi.org/10.1175/JCLI-D-14-00565.1>
- 504 Virts, K. S., Wallace, J. M., Hutchins, M. L., & Holzworth, R. H. (2015). Diurnal and Seasonal
505 Lightning Variability over the Gulf Stream and the Gulf of Mexico. *Journal of the*
506 *Atmospheric Sciences*, *72*(7), 2657–2665. <https://doi.org/10.1175/JAS-D-14-0233.1>
- 507 Watters, D., & Battaglia, A. (2019). The Summertime Diurnal Cycle of Precipitation Derived
508 from IMERG. *Remote Sensing*, *11*(15), 1781. <https://doi.org/10.3390/rs11151781>
- 509 Worku, L. Y., Mekonnen, A., & Schreck, C. J. (2019). Diurnal cycle of rainfall and convection
510 over the Maritime Continent using TRMM and ISCCP. *International Journal of*
511 *Climatology*, *joc.6121*. <https://doi.org/10.1002/joc.6121>
- 512 Xie, S., Neelin, D., Bechtold, P., & Ma, H.-Y. (2018, June 24). Improving the simulation of
513 diurnal and sub-diurnal precipitation over different climate regimes.
514 WCRP/GEWEX/GASS. Retrieved from <https://portal.nersc.gov/project/capt/diurnal/>
- 515 Yokoi, S., Mori, S., Katsumata, M., Geng, B., Yasunaga, K., Syamsudin, F., et al. (2017).
516 Diurnal Cycle of Precipitation Observed in the Western Coastal Area of Sumatra Island:
517 Offshore Preconditioning by Gravity Waves. *Monthly Weather Review*, *145*(9), 3745–
518 3761. <https://doi.org/10.1175/MWR-D-16-0468.1>
- 519 You, Y., Meng, H., Dong, J., & Rudlosky, S. (2019). Time-Lag Correlation Between Passive
520 Microwave Measurements and Surface Precipitation and Its Impact on Precipitation
521 Retrieval Evaluation. *Geophysical Research Letters*, *46*(14), 8415–8423.
522 <https://doi.org/10.1029/2019GL083426>
523 |

524 *Figure 1. Number of observations for sun-synchronous PMW sensors (top) and mean*
525 *precipitation rate for IMERG V05B and V06B (bottom) as a function of LST hour from*
526 *December 2014 to February 2015 over the Southern Ocean latitudes (40–60°S), where actual*
527 *diurnal variability should be minimal.*

528 *Figure 2. The LST hour of the peak in low-pass filtered mean precipitation rate at every 0.1°*
529 *over the conterminous United States during June-July-August from 2014 to 2018 in (a) IMERG*
530 *and (b) MRMS; (c) the histogram of the difference in the peak LST hour for grid boxes in the*
531 *outlined southeastern US states; and (d) unfiltered (black) and low-pass filtered (gray) mean*
532 *precipitation rates of the outlined southeastern US states in IMERG (solid line) and MRMS*
533 *(dashed line) as a function of LST.*

534 *Figure 3. The LST hour of the peak in low-pass filtered mean precipitation rate of IMERG at*
535 *every 0.1° over the Maritime Continent during March-April-May from 2001 to 2018.*

536 *Figure 4. Mean precipitation rate during different months of the year for (a) Singapore, (b)*
537 *Bangladesh, and (c) Lake Victoria in Africa from 2001 to 2018.*

Figure 1.

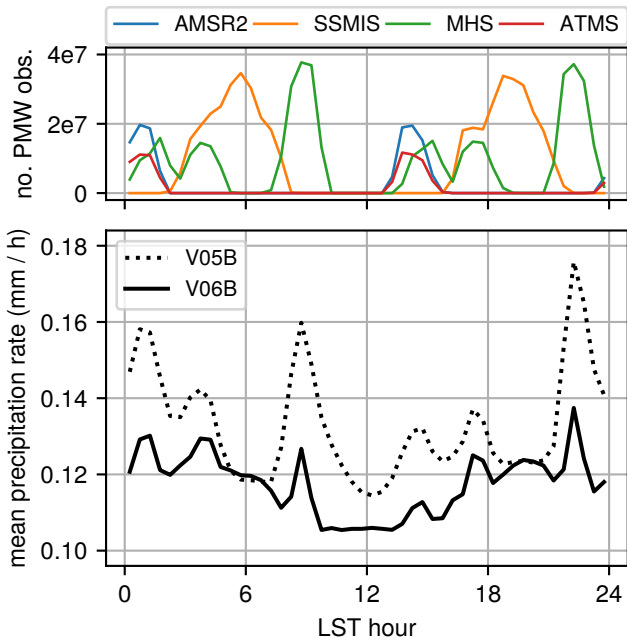


Figure 2.

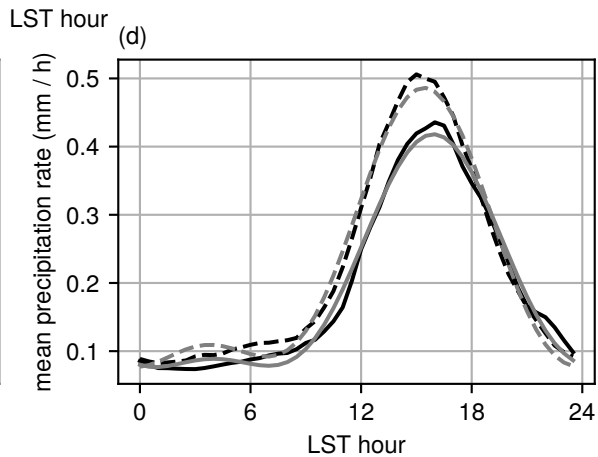
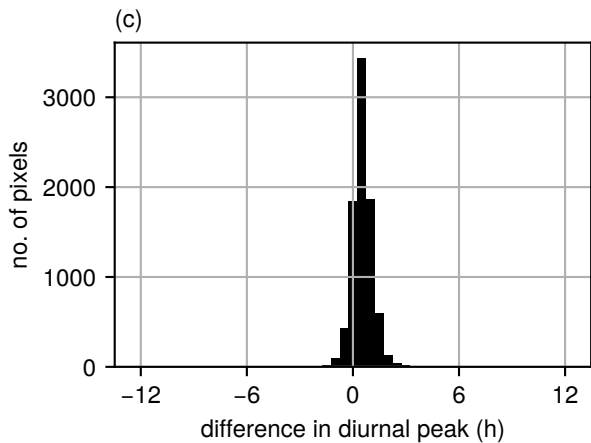
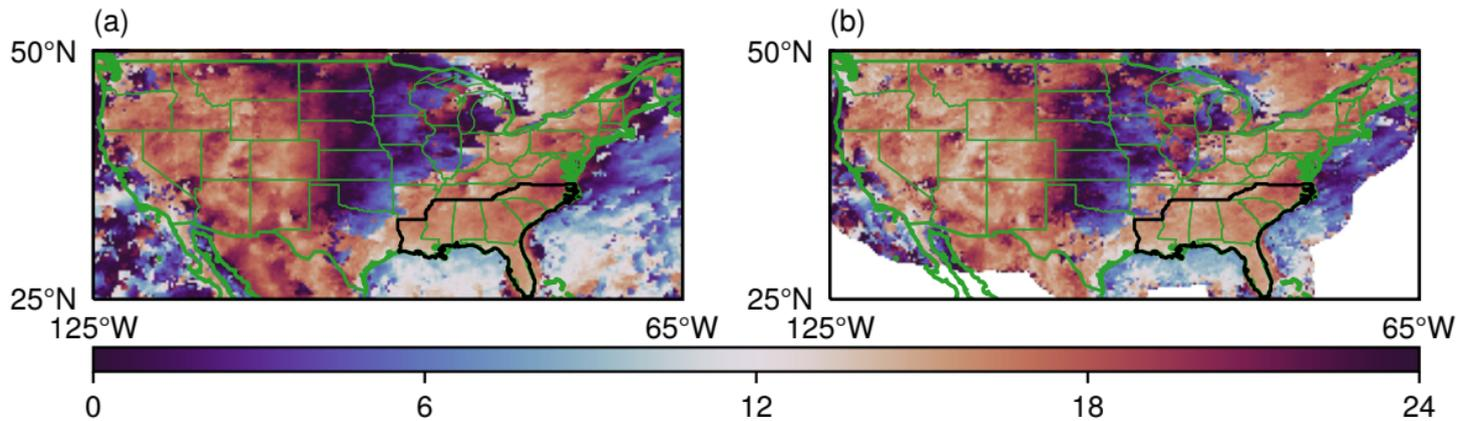


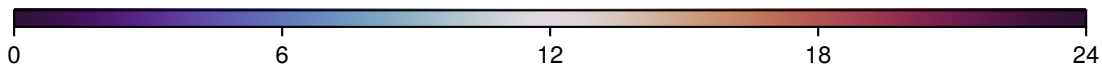
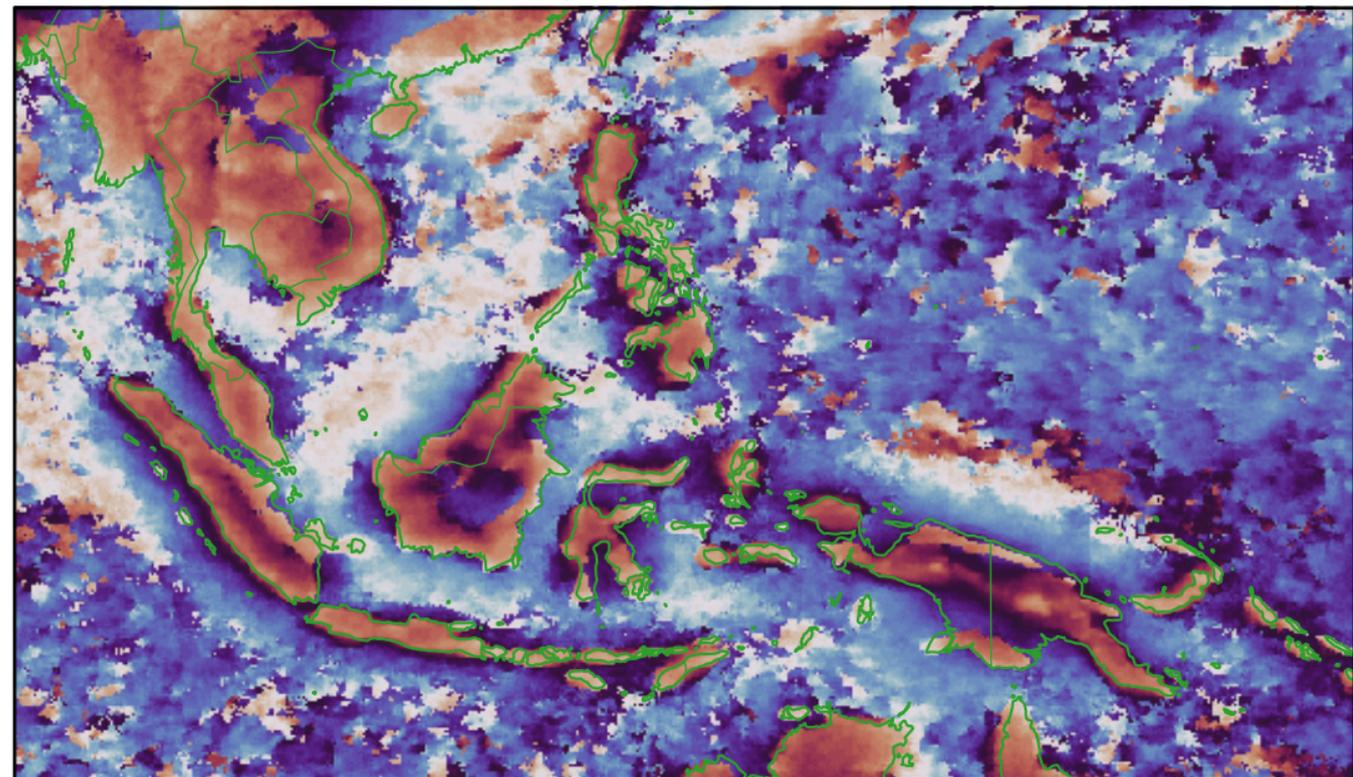
Figure 3.

25°N

15°S

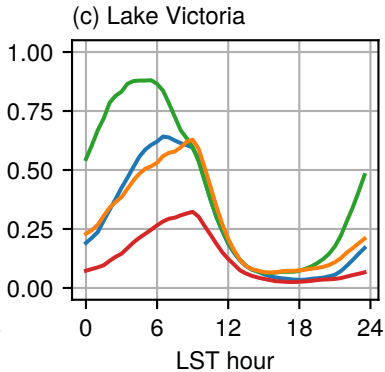
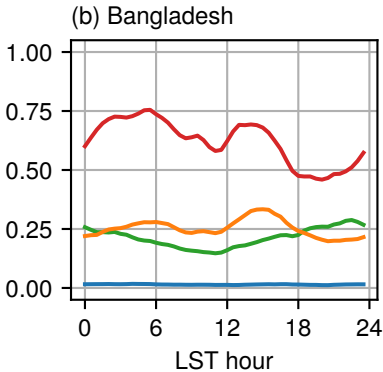
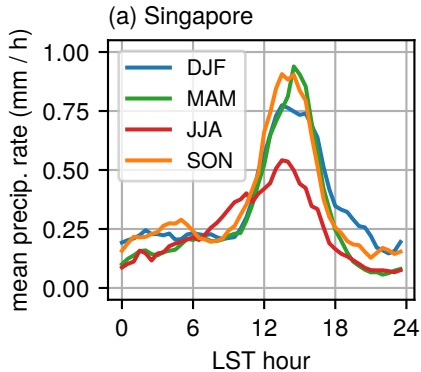
90°E

160°E



LST hour

Figure 4.



Geophysical Research Letters

Supporting Information for

Diurnal Cycle of IMERG Vo6 Precipitation

Jackson Tan^{1,2}, George J. Huffman², David T. Bolvin^{2,3}, and Eric J. Nelkin^{2,3}

¹ Universities Space Research Association, Columbia, Maryland.

² NASA Goddard Space Flight Center, Greenbelt, Maryland.

³ Science Systems and Applications, Inc., Lanham, Maryland.

Contents of this file

Text S1
Figures S1 to S8

Introduction

This supporting information provides some supplementary information on the method used in the study to identify IMERG grid boxes in different countries as well as on results that justify and augment some of the statements in the text.

Text S1.

The IMERG grid boxes were identified with Singapore, Bangladesh, and Lake Victoria (Figures S5–7) using Esri shapefiles, determined by whether the coordinates of the center of the grid box falls within the boundary of the geometrical polygon. For Singapore, the shapefile used was from the Urban Redevelopment Authority Master Plan 2014 Planning Area Boundary (No Sea) dataset. For Bangladesh, the shapefile used was from the ArcGIS Countries WGS84 dataset. For Lake Victoria, the shapefile used was from the Natural Earth lakes dataset.

In the case of Singapore, the grid boxes north and south of the three selected ones (Figure S2) have a substantial fraction of their area within the boundaries of Singapore as well as in the neighboring Malaysia and over the water.. While it can be argued that these grid boxes should

be identified in an analysis over Singapore, we excluded them in this study because of our intention in demonstrating the capability of IMERG in analyzing regions of very limited extent.

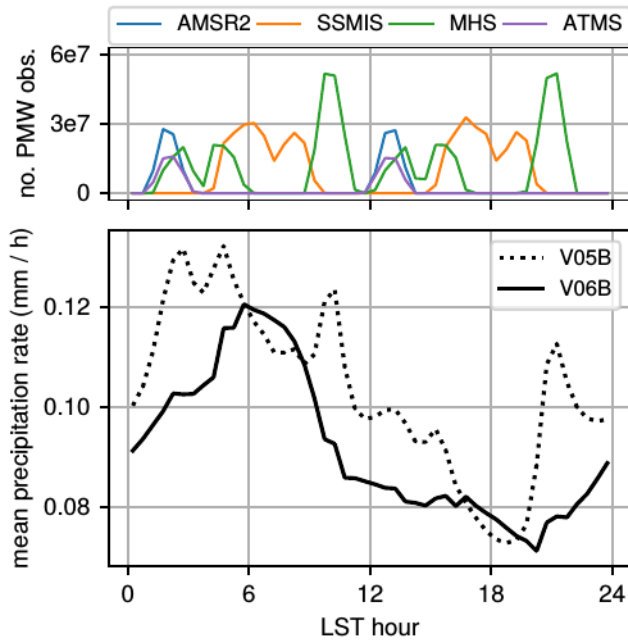


Figure S1. Similar to Figure 1, but over the northeast Pacific (180–130°W, 30–50°N) in June–July–August of 2014.

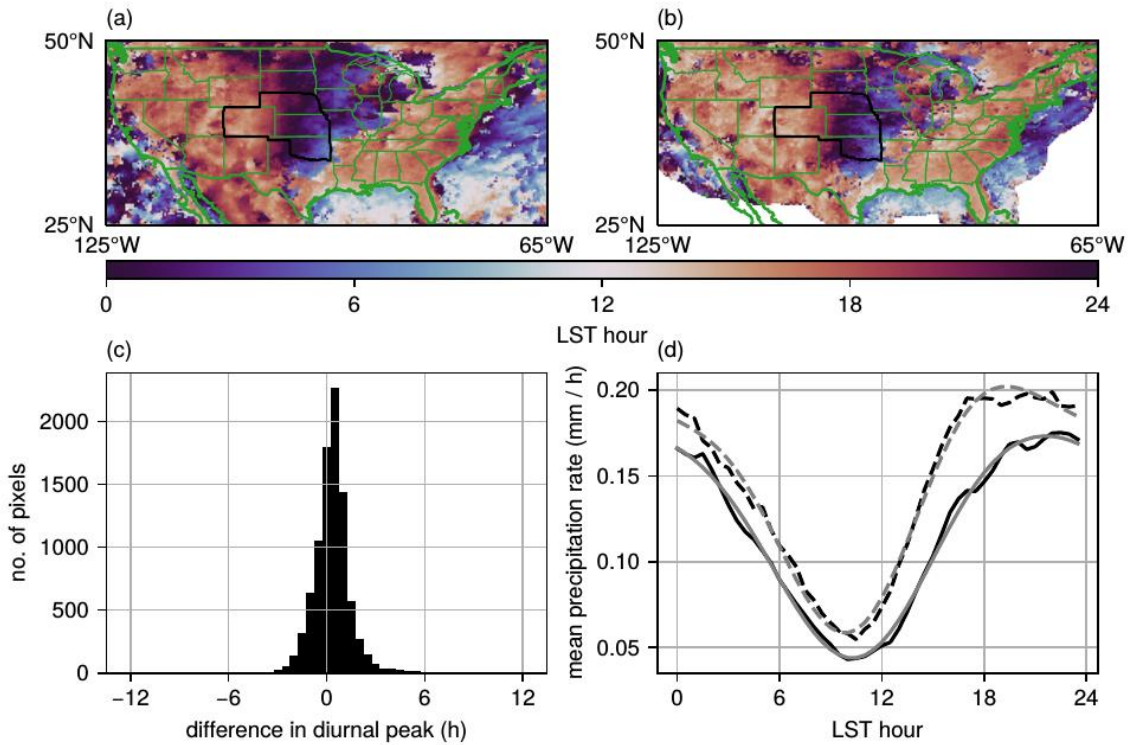


Figure S2. Similar to Figure 2, but over the central US states. For the difference in diurnal peaks (c), the mean is +0.33 h, the median is +0.5 h, and the interquartile range is -0.5 h to +1.0 h.

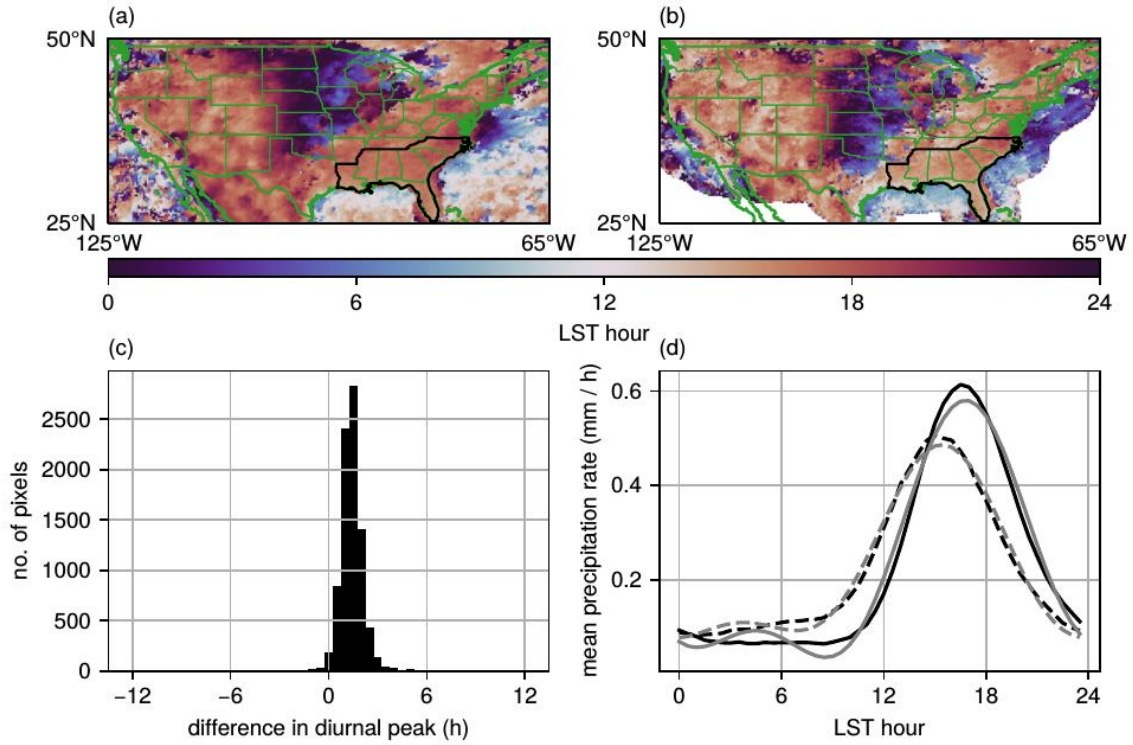


Figure S3. Similar to Figure 2, but for IR precipitation in the IMERG files instead of gauge-adjusted precipitation. For the difference in diurnal peaks (c), the mean is +1.48 h, the median is +1.5 h, and the interquartile range is +1.0 h to +2.0 h.

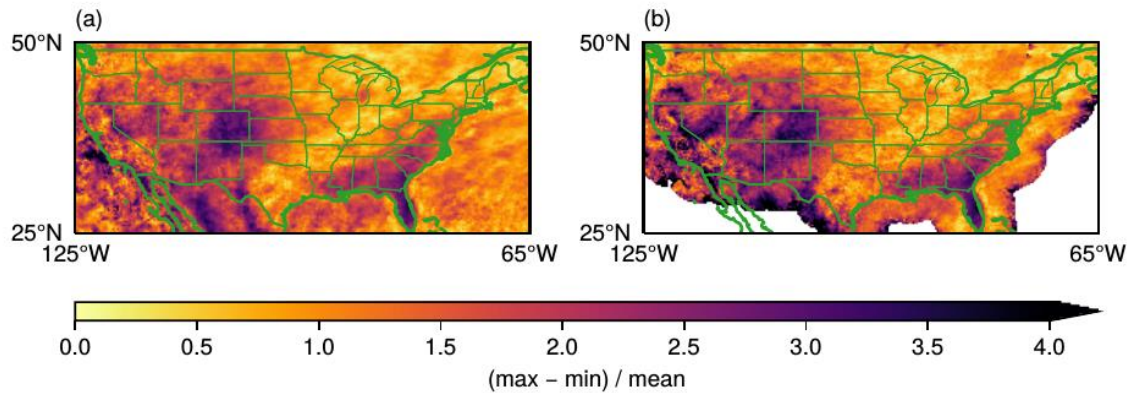


Figure S4. The normalized diurnal amplitude of (a) IMERG and (b) MRMS, expressed as the difference between the difference between the maximum and minimum low-pass filtered precipitation rate divided by its mean at each grid box.

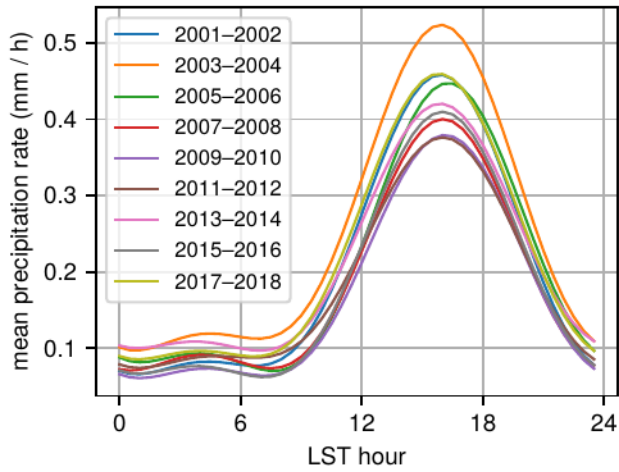


Figure S5. Low-pass filtered mean precipitation rates of the southeastern US states (outlined in Figure 2a and 2b) in IMERG as a function of LST over every two-year period in the IMERG record.

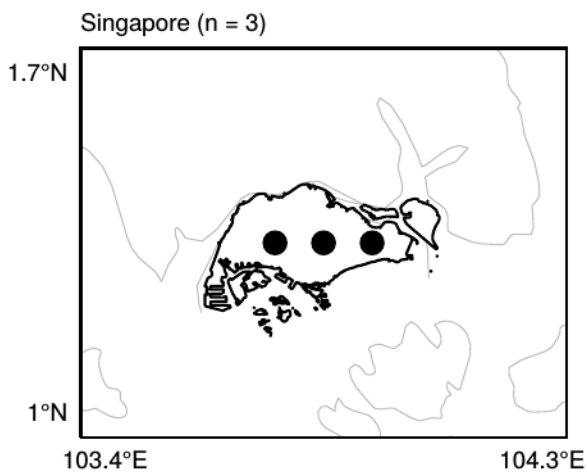


Figure S6. Center of IMERG grid boxes (dots) falling within the land boundary of Singapore. n indicates the total number of grid boxes.

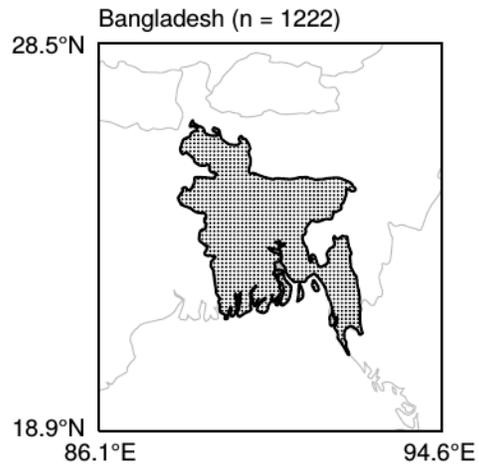


Figure S7. Similar to Figure S5, but for Bangladesh.

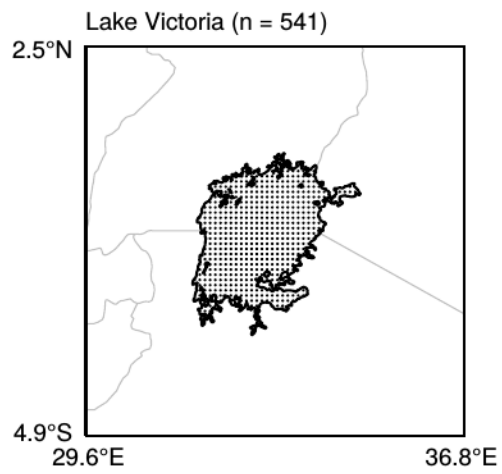


Figure S8. Similar to Figure S5, but for Lake Victoria in Africa.